Strong Storm-effect behaviors of topside and bottom-side ionosphere under low solar activity: Case study in the geomagnetic storm during 25-27 August 2018

Wang Li[1,2], Dongsheng Zhao[2*], Changyong He[3], Shen Yi[4], Craig M. Hancock[5], Kefei Zhang[2]

[1] Faculty of land resources engineering, Kunming University of Science and Technology, Kunming, China.

[2] School of Environmental Science and Spatial Informatics, China University of Mining and Technology, Xuzhou, China.

[3] National-Local Joint Engineering Laboratory of Geo-Spatial Information Technology, Hunan University of Science and Technology, Xiangtan, China.

[4] Key Laboratory for Synergistic Prevention of Water and Soil Environmental Pollution, Xinyang Normal University, Xinyang, China.

[5] School of Architecture, Building and Civil Engineering, Loughborough University, Loughborough, United Kingdom.

Corresponding author: Dongsheng Zhao (dszhao_gnss@foxmail.com)

Key points:

- First time to give an overview of the development of global Rate of total electron content (TEC) Index change in the whole phase of storm
- Positive ionospheric plasma irregularities in the altitudes of 100 to 150km were only detected near Auroral zone (> ~50°N/S)
- Low-middle latitude plasma irregularities were a combined action of density ratio O/N_2, equatorial electrojet and vertical E×B drift

Abstract

The 25-27 August geomagnetic storm was the third largest storm in 24th solar cycle, which was a surprising space event that generated in the background of very low solar activity. This study presents an overview of temporal-spatial behaviors of ionospheric plasma irregularities as functions of geographic longitude, latitude and altitude by ground-based (GNSS receivers and ionosonde) instruments and space-borne (Swarm-A and Swarm-B) satellites. The results not only reveal the enhanced equatorial ionization anomaly (EIA) and hemispheric asymmetry over the Asian-Australian and American sectors in a particular time, but also discover the development of hemispheric asymmetric features of global ROTI in the main and recovery phases. In addition, this storm also triggered positive plasma irregularities in altitudes of 100 to 150km near Auroral zone, and the changed ratio of bottom-side plasma irregularities exceeded 250%, which has been cross validated by multiple instrument and TIE-GCM's simulation. Furthermore, the thermospheric density ratio O/N_2, equatorial electrojet and vertical E×B drifts suffered from the storm largely, the equatorial and mid-latitude plasma irregularities may be a combined action of thermospheric composition change, equatorial electrojet and vertical E×B drifts. Finally, the storm also induced positive Joule heating irregularities in Auroral ionosphere in altitudes of 100 to 400km with a maximum changed ratio of >200%, as well as the cross Polar voltage enhanced to ~90kv. The Polar ionospheric irregularities may be associated with the additional energy input through the ways of particle precipitation, Joule heating and ionospheric currents intensification.

Key words: ionospheric disturbances, geomagnetic storm, hemispheric asymmetry, TIE-GCM, O/N_2

Plain language: Large amounts of charged particles deposited in the thermosphere-ionosphere system during a strong geomagnetic storm, this process could change global ionospheric convection and weaken the activities of positioning, navigation, radio communication, etc. This study tries to discover the spatial-temporal changes of global ionosphere under the strong geomagnetic storm during 25-27, August 2018. From the observations of Global Navigation Satellite System (GNSS) receivers and radars, we first time to discover the spatial-temporal evolutions of global plasma irregularities, and reveal the storm-enhanced equatorial ionization

anomaly and hemispheric asymmetry in the Asian-Australian and American sectors. Besides, positive plasma irregularities in the altitudes of 100 to 150km were only near Auroral zone (> ~50°N/S), rather than in low-middle latitudes. Furthermore, the potential drivers are investigated for explaining the plasma irregularities. The equatorial and mid-latitude irregularities may be a combined action of thermospheric composition change, equatorial electrojet and vertical E×B drifts. The Polar ionospheric irregularities may be associated with the additional energy input through the ways of particle precipitation, Joule heating and ionospheric currents intensification.

1. Introduction

Ionosphere has a serious effect on absorbing, scattering and refracting radio signals, which is a main error source in the navigation and positioning service. Now the global navigation satellite system (GNSS) differential technique and empirical/theoretical models are usually used to correct the ionospheric delay. However, ionospheric plasma during severe geomagnetic storms suddenly increases or decreases violently, which easily reduces the accuracy of positioning and navigation. Now available techniques are not good at correcting severe storm-effect ionospheric perturbations; therefore, it is necessary and valuable to investigate the ionospheric spatial-temporal behaviors response to strong magnetic storms and to discuss the probable drivers.

Geomagnetic storm usually has a severe effect on the ionospheric system, auroral particle precipitation, Polar ionospheric currents and convection are reinforced largely during a geomagnetic storm. The enhanced Polar ionospheric ionization and electric fields penetrate to low-middle latitudes, this process affects global electrodynamics and changes the structure of the thermospheric-ionospheric system remarkably. The Joule heating and Auroral particle precipitation heat and expand the thermosphere, which further changes the composition and dynamics of the thermospheric-ionospheric system [*Astafyeva et al.*, 2015]. With rapid development of Global Navigation Satellite System (GNSS) and radio occultation, the storm-effect ionospheric behaviors have been paid more attention by multiple ground-based and space-borne techniques. The “Halloween” storm erupted on 29-30, October 2003 was one of strongest geomagnetic storms in this century. After a few hours when the interplanetary

magnetic field suddenly turned southward, the dayside ionospheric total electron content (TEC) increased about 40%, and the Challenging Minisatellite Payload (CHAMP) profiles indicated the dayside TECs over mid-latitudes increased ~900% on 30 October [*Mannucci et al.*, 2005]. The significant increments of TEC and peak density (NmF2) were also observed over the European and North African sectors during a following stronger geomagnetic storm occurred on November 20, 2003[*Crowley et al.*, 2006]. Moreover, the sudden ionospheric irregular behaviors response to geomagnetic storms were also been reported over Jicamarca [*Zhang et al.*, 2019], Brazilian equatorial–low latitudes [*de Paula et al.*, 2019], China and adjacent areas [*Aa et al.*, 2018], Asian-Australian sector [*Lei et al.*, 2018], Indian sector [*Ramsingh et al.*, 2015], Turkey [*Karatay*, 2020], Arctic and Antarctic [*Durgonics et al.*, 2017; *Mitchell et al.*, 2005; *Shreedevi et al.*, 2020] and in a global scale [*Atıcı and Sağır*, 2020; *Li et al.*, 2022]. These reports revealed that strong geomagnetic storms easily triggered large-scale positive or negative traveling ionospheric disturbances (TIDs), and sometimes the TIDs had a significant latitudinal asymmetric structure in northern-southern hemispheres that is caused by the displaced magnetic poles and seasonal asymmetries in the thermosphere-ionosphere system. Multi-instruments observations and theoretical model simulations were conducted for explaining the disturbed ionospheric dynamic convections, and the results concluded that the negative TIDs were primarily attributed to a decrement of the thermospheric density ratio O/N_2 [*Dmitriev et al.*, 2017; *Fuller‐Rowell et al.*, 1994]. However, the drivers for positive TIDs were various, thermospheric neutral winds, disturbance dynamo electric fields (DDEF), prompt penetration electric field (PPEF) as well as charged particle precipitation, had been reported to be the potential factors in enhancing plasma densities [*Atıcı and Sağır*, 2020; *Crowley et al.*, 2006; *Nava et al.*, 2016; *Qian et al.*, 2019; *Richmond and Lu*, 2000].

Ionospheric storms primarily occur as a consequence of strong coronal mass ejection (CME), such as the magnetic storms in 22-23, June 2015 [*Ngwira et al.*, 2019] and 7-8, September 2017 [*Li et al.*, 2018a]. However, the 25-27, August 2018 space event that is the third largest magnetic storm in 24^{th} solar cycle happened after a slowly moving CME on 20 August, it is a huge surprise that the weak CME that even didn't show a sudden impulse could trigger a strong ionosphere-thermosphere response. The positive and negative ionospheric perturbations over North America [*Cherniak and Zakharenkova*, 2022], Brazil [*Spogli et al.*,

2021], Asia [*Lissa et al.*, 2020], Middle latitudes [*Chang et al.*, 2022], as well as the global [Astafyeva *et al*., 2020] response to the surprising space event have been reported. This geomagnetic storm induced penetration electric fields created favorable conditions for strong fountain effect enhanced equatorial ionization anomaly (EIA) and generated equatorial plasma bubbles (EPBs). The EPBs appeared over a larger latitudinal extent of EIA crests, while the plasma density in the western coast of North America depleted in the northwestward direction [Cherniak and Zakharenkova, 2022]. The Defense Meteorological Satellite Program (DMSP) also detected midlatitude plasma depletion in the Asian sector, the local TIDs were responsible for the midlatitude plasma depletion in Asia and United States, rather than the absence of EPBs [Chang *et al*., 2022]. Different from the mid-latitude plasma depletion in the northern hemisphere, Spogli et al. [2021] used the situ measurements provided by China Seismo-Electromagnetic Satellite and by Swarm-A satellite with ground-based observations to reveal the ionospheric response at low-middle latitudes over Brazil, and found that significant foF2 increments appeared over the ionosondes located at both of dip-equator and southern crest of the EIA. The decrease of the eastward electric field was the main driver for the equator station, while it was resulted from the storm-induced equatorward thermospheric winds for the crest station. In addition, unprecedented hemispheric asymmetries of the thermospheric-ionospheric responses were also observed during the main and recovery phases of the storm, which expressed that strong positive plasma storms occurred in the northern hemisphere at the beginning of the space event, while an extreme expansion of the thermospheric composition ratio O/N_2 appeared in the opposite hemisphere during the recovery phase. The seasonal asymmetry in the high-latitude plasma and neutral mass density distributions along with the asymmetries in the geomagnetic field played a decisive role for the hemispheric asymmetric structure of disturbed plasma [*Astafyeva et al.*, 2020].

Most of previous studies focused on the planar ionospheric response (TEC) to the storm, but the altitudinal plasma behavior was still not clear. Besides, the storm-effect ionospheric response is controlled by multiple drivers at a particular moment of time and in particular location. The present study has the objectives to examine: (1) the development of hemispheric asymmetry of plasma irregularities in the main and recovery phase; (2) the altitudinal behaviors of plasma irregularities in low-middle latitudes and auroral zone; (3) the potential drivers for

the latitudinal plasma irregularities over the Asian-Australian and American sectors. To address these objectives, the latitudinal ionospheric irregularities are detected by a set of ground-based (GNSS receiver and digital-ionosonde) and space-borne (SWARM) instruments, and the potential drivers for the equatorial-auroral irregularities are discussed by a set of magnetometer, SuperDARN, Global Ultraviolet Imager (GUVI) and TIE-GCM's simulation.

2. Datasets

In order to analyze planar-vertical behaviors of global plasma irregularities during the magnetic storm on 25-27, August 2018 completely, the ground-based (GNSS receiver and ionosonde) observations and the plasma profiles derived from the space-borne Swarm constellation are used. In addition, the horizontal components of the magnetic field, thermospheric density ratio O/N_2 and the TIE-GCM's simulations are also adopted for explaining the drivers of plasma irregularities. The geographic locations of ground-based instruments are shown in Figure 1, and more detail information of several kinds of datasets are introduced as follows.

The GNSS observations are obtained from the University NAVSTAR Consortium (UNAVCO) that provides access to geodetic GPS/GNSS data used for geoscience research and education. The UNAVCO provides about 2500 Receiver Independent Exchange Format (RINEX) files daily through the link https://www.unavco.org/data/gps-gnss/gps-gnss.html. It should be noted that the vertical total electron content (VTEC) estimated by the carrier-phase smoothed pseudo-range method is used to investigate the ionospheric perturbations during the geomagnetic storm [*Li et al.*, 2018b]. For similarity, the TEC signifies VTEC in the whole study. In addition, two chain digital-ionosondes located at the Asian-Australian and American sectors are also utilized to investigate the vertical behaviors of storm-induced plasma irregularities. Due to the influence of geomagnetic storm, the digital-ionosonde in the Asian sector fails to observe the auroral plasma irregularities. The ionosonde PQ052 (14.6°E, 50°N) located at Pruhonice in Europe is selected. The sounder profiles of two chains can be obtained from the Lowell DIDBase (jdbc:firebirdsql://didbase.giro.uml.edu/didb) via the SAO explorer.

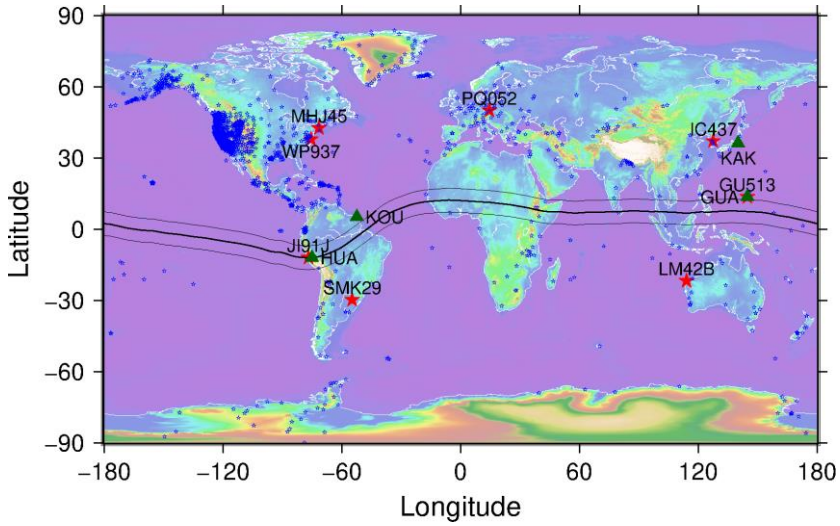

Figure 1. Spatial distribution of GNSS stations, ionosondes and magnetometers. The blue pentagrams signify global GNSS stations, the red pentagrams signify the ionosondes located at the Asian-Australian and American sectors, the green triangles signify magnetometers, and the solid and dashed curves depict the location of the magnetic equator and the region of equatorial electrojet.

Swarm consists of three microsatellites (Alpha, Bravo and Charlie) that are placed in two different orbital planes, among them the Swarm-A and Swarm-C fly at a mean altitude of 450km, and the satellite Swarm-B places in a mean altitude of 530km. In this study, the electron density profiles of Swarm-A and Swarm-B are selected to analyze the plasma irregularities, and the electron density is derived from the high gain ion current that is determined by the Langmuir probe. The Swarm profiles can be obtained from the website https://swarmdiss.eo.esa.int/#swarm%2FLevel2daily%2FEntire_mission_data%2FTEC%2FTMS. In addition, the daily F10.7 index, 81-day mean F10.7 and Kp index are imported to the TIE-GCM model as input parameters, and the output parameters include electron density, neutral winds, thermospheric composition and electric field. More details about the TIE-GCM, the readers please refer to https://www.hao.ucar.edu/modeling/tgcm/tie.php. For improving the simulated accuracy of the TIE-GCM products response to geomagnetic storms, the period of the TIE-GCM products is from 00:00 (Universal Time, UT), 23 August to 29 August 2018.

3. Results

3.1 Solar-terrestrial environment

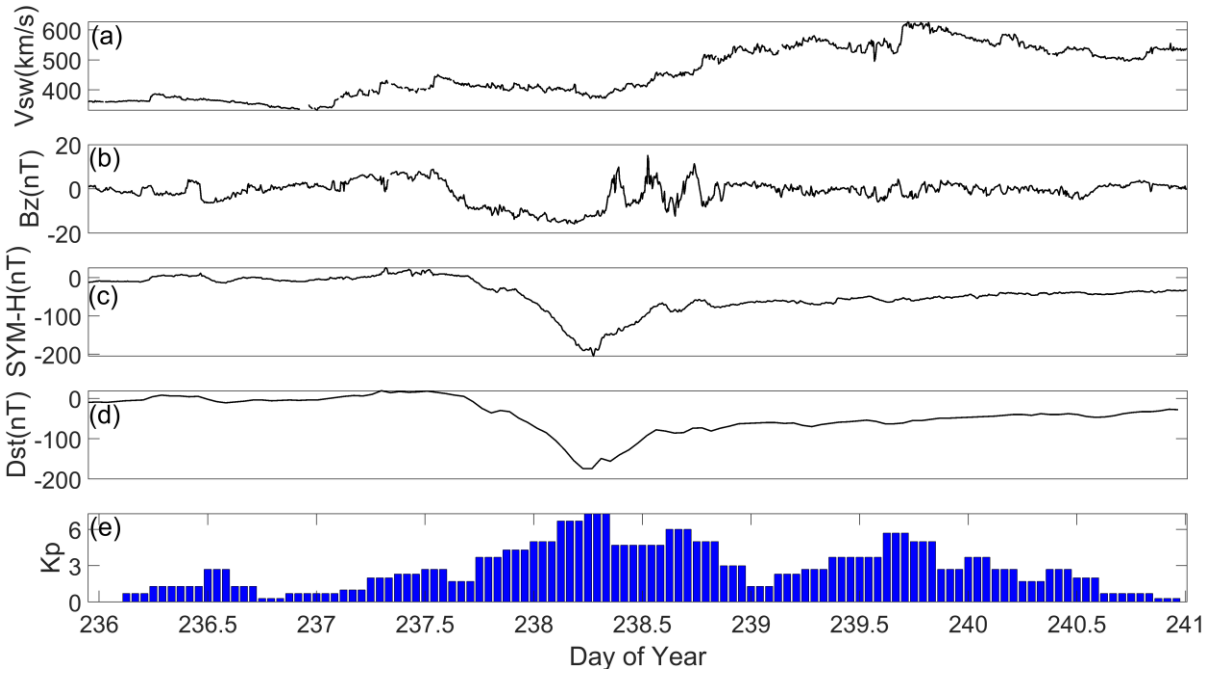

Figure 2. Variations of solar-terrestrial indices during day of year (DOY) 236 to 240 in 2018

Solar-geomagnetic change is an important factor in effecting the process of ionospheric plasma irregularities during storms. Therefore, the data of solar wind speed (Vsw), interplanetary magnetic field, and geomagnetic indices obtained from the Goddard Space Flight Center (https://omniweb.gsfc.nasa.gov/form/dx1.html) is analyzed. The record third largest geomagnetic storm in the 24th cycle was initiated from a slow CME on 20 August 2018, which arrived at the earth thermosphere-ionosphere system on 25 August. As shown in Figure 2, the solar-terrestrial indices were in a quiet level before UT14, DOY 237 (25 August), and a strong geomagnetic storm happened from UT14, DOY237 to DOY 239 (27 August). Figure 2(a) shows the Vsw was low with a mean velocity of 400 to 450km/s in the main phase (UT14, DOY237 - UT7, DOY238) of the geomagnetic storm, while it enhanced abruptly in the recovery phase with a maximum speed of 620km/s. Figure 2(b) shows the Bz component of interplanetary magnetic field (IMF) had an abrupt southward excursion. From UT14, DOY237, the Bz turned southward with a minimum value of -18nT in the forenoon of DOY 238. The horizontal component of longitudinally symmetric disturbances (SYM-H) is essentially the same as the Dst index to describe the mid-latitude geomagnetic disturbances. Figure 2(c) and 2(d) express that both SYM-H and Dst had a significant negative excursion since the afternoon of DOY 237, and these indices reached to minimum values of ~-200nT and ~-180nT at UT06-

08, DOY 238, respectively. As well as the global geomagnetic field indexed by Kp enhanced to a maximum level of 7. According to the classification of geomagnetic storm released by National Oceanic and Atmospheric Administration (NOAA), this storm is classed as “strong”.

3.2 Ionospheric irregularities over the Asian-Australian and American sectors

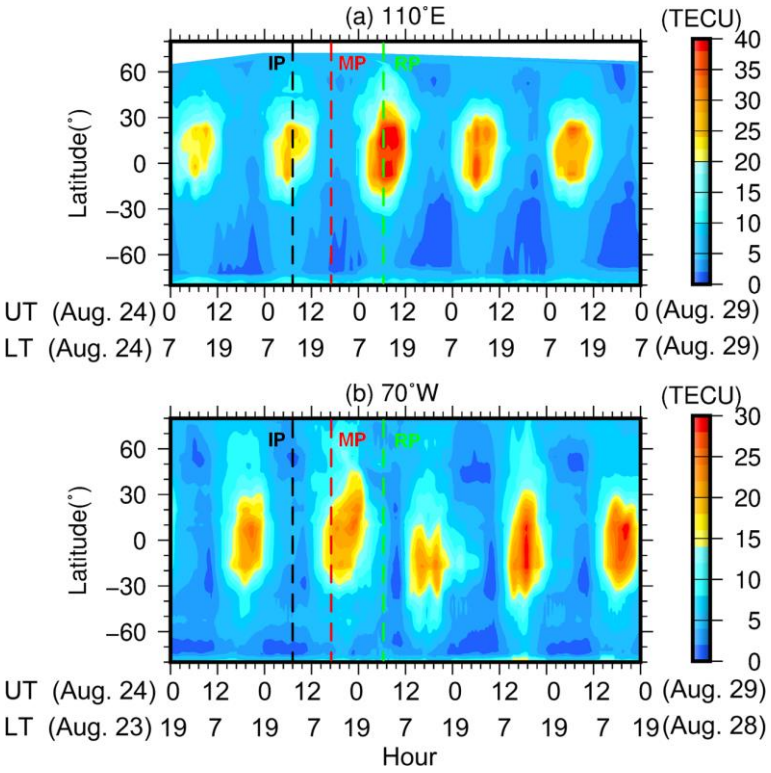

Figure 3. Latitudinal TEC changes along (a) 110°E, (b) 70°W longitudes during August 24-28, the dashed black line signify the initial phase (IP) of the geomagnetic storm, the dashed red line signify the main phase (MP), and the dashed green line signify the recovery phase (RP). White color depicts empty cells due to lack of actual observations.

The dual-frequency observations of about 2500 GNSS receivers provided by UNAVCO are used to estimate the global TEC map, then the TEC grid maps are constructed by Kriging interpolation method. The north-south cross-sections (keograms) of the GNSS TEC maps along the 110°E and 70°W longitudes during 24-28 August are plotted to illustrate the temporal evolution of the storm-effect TEC changes over two sectors. These keograms, plotted as a function of UT time and geographic latitude, as shown in Figure 3. Figure 3(a) demonstrates that in the Asian-Australian sector, the ionospheric TEC kept in a low level of 20 to 25TECU. In the main phase of the storm, the equatorial ionospheric TEC enhanced significantly with a

double peak structure that coincided to the Dst index decreased to a maximum value of -174nT. The enhanced TEC primary occurred in the ending of main phase and the beginning of recovery phase (UT04-10, 26 August), the maximum TEC reached to 40TECU.

Different from the TEC change over the Asian-Australian sector, Figure 3(b) found a significant hemispheric asymmetric structure of TEC irregularity in the American sector. For example, significant TEC depletion happened over the American sector in the recovery phase. In the afternoon of 26 August, the TEC in the northern hemisphere depleted from 15-20TECU to 10TECU, while the equatorial and mid-latitude TEC in the opposite hemisphere enhanced about 5TECU. The positive TEC storm was stronger in the afternoon of following two days, and the maximum enhanced TEC exceeded 30TECU. Figure 3 concludes that the geomagnetic storm triggered an asymmetric ionospheric storm, and the occurred phases of ionospheric storm over different longitudes had a particular diversity.

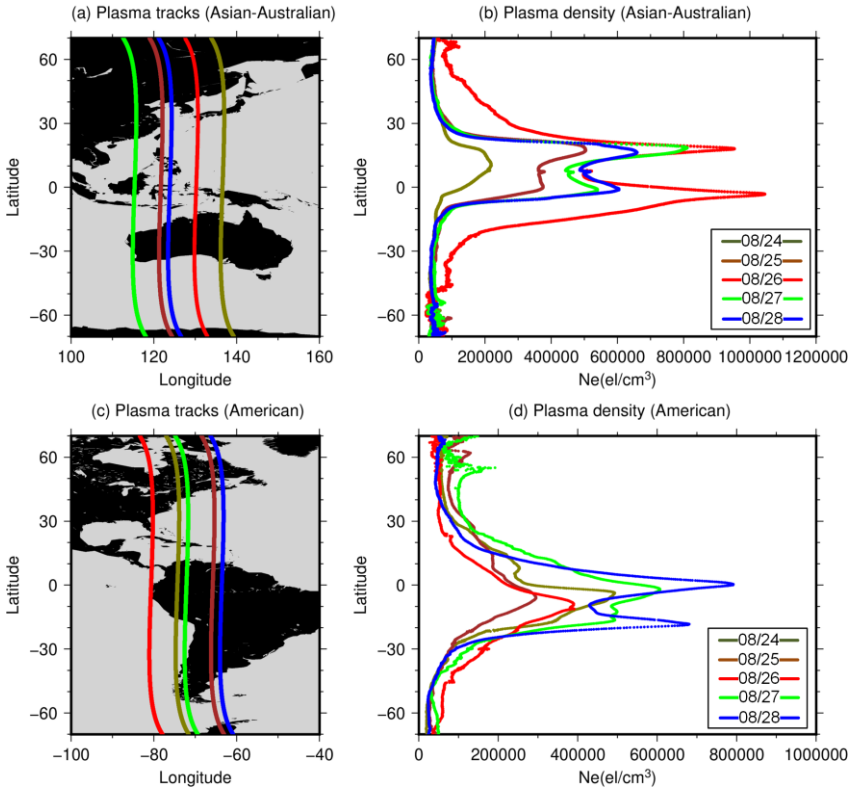

Figure 4. Daily changes of Ionospheric electron density detected by Langmuir probe instrument onboard Swarm-A satellite during (a-b) the main phase over the Asian-Australian sector (c-d) and the recovery phase over the American phase from 24 to 28 August.

Figure 4 gives an overview on the daily development of storm-effect ionospheric electron density (Ne) as measured by the space-borne Swarm-A satellite that flies at an orbital altitude

of ~450km. Here, the electron density signifies the amounts of plasma at the Orbital altitude of Swarm-A, which is useful to reveal the change of topside ionosphere during the storm. The result in Figure 3 demonstrates that the storm-induced plasma irregularities over the Asian-Australian sector was larger in the main phase, but in the recovery phase, the American sector was larger. Therefore, five Ne profiles derived from Swarm-A during 24-28 August are plotted to describe the Asian-Australian ionospheric response during the main phase. These profiles not only have an adjacent longitude in ~120°E to 140°E span, but also have a nearly observed time within UT05:10 to UT06:30, as shown the Ne tracks in Figure 4(a). Figure 4(b) shows the variation of daily Ne profiles as a function of geographic latitude, we can find that the plasma density kept in a low level with the peak density of $\sim 5 \times 10^5$el/cm^3 during 24-25 August. In the main phase, the topside Ne over the Asian-Australian sector significantly enhanced. The red curve expresses a significant structure of EIA on 26 August, the double plasma crests located at the 10°N to 20°N and 0° to 10°S latitudinal spans, respectively. Compared to the background values, the storm-enhanced Ne increased ~2 times with a maximum value of $\sim 1.05 \times 10^6$el/cm^3. The enhanced EIA is believed caused by a daytime "superfountain" effect that driven by the PPEFs. During strong geomagnetic storms, the PPEFs of eastward polarity could largely uplift the equatorial ionosphere over the sunlit and post-sunset sectors that drive the equatorial plasma along the geomagnetic field line to higher altitudes and expanded poleward latitudes with a significant enhancement of the EIA [Cherniak and Zakharenkova, 2022]. In the following two days, the intensity of EIA gradually decreased to a normal level.

Different from the sudden enhanced TECs over the Asian-Australian sector, the TEC's change over the American sector in the main phase (25-26 August) was not significant. However, remarkable TEC enhancements were observed in the recovery phase, especially on 28 August, the peak density occurred in the North America with a value of $\sim 8 \times 10^5$el/cm^3. The hemispheric asymmetric structure of ionospheric TEC agrees well with the observations of ground-based radars and space-borne Swarm-A. Finally, the TEC's changes over both the Asian-Australian and American sectors reveal that the magnetic storm not only enhanced the equatorial plasma density, but also triggered drastic polar ionospheric disturbances. The development of storm-induced polar ionospheric disturbances will be investigated in the following section.

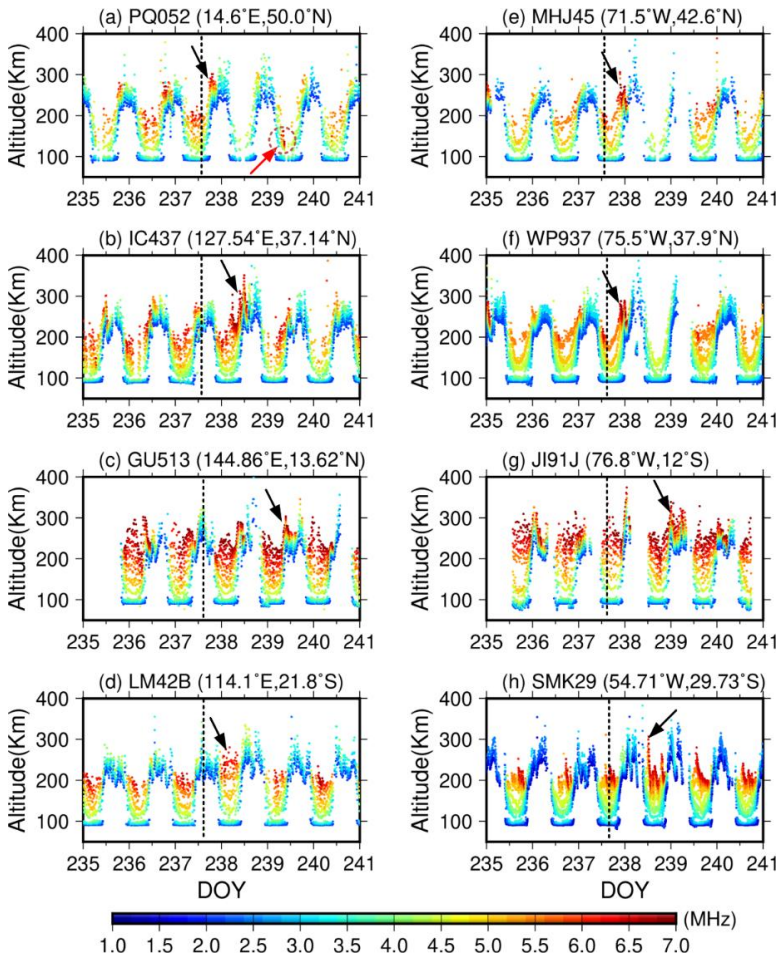

Figure 5. Vertical sounder profiles of two chain ionosondes located at the Asian-Australian (left) and American sectors in a whole phase of geomagnetic storm, the dashed line signifies the onset of the main phase of the storm

An ionosonde sounder is a radar that sweeps the high-frequency (HF) band signals and receives the echoes for examing the ionosphere and monitoring HF propagation conditions. Ionosonde primarily operates between 1.6MHz to 12 MHz. With this advantage, the two ionosonde chains located at the Asian-Australian and American sectors could detect the vertical dynamic propagation of storm-induced plasma irregularities, the results as shown in Figure 5. From the left panels, the radars located at the Asian-Australian sector detected HF signals with frequencies between 5.5 to 7MHz in the midnight-dawn (for local time, it was around the noon) during DOY235-240, and the HF signals accumulated under 200km. The equatorial radar detected HF plasma signal accumulated at a higher altitude. For example, Figure 5(c) shows the ionosonde GU513 located at the Guam measured a maximum frequency of 7MHz around the altitude of 250km in a minor solar-geomagnetic activity. After the onset of geomagnetic

storm, the plasma density during the midnight-dawn in the next day (26 August) suddenly enhanced and uplifted. As shown in the black arrows, enhanced HF plasma density were all detected over the equatorial and midlatitude radars (IC437, GU513, LM42B) in the main phase. Especially over the radar IC437, the peak height of ionosphere was uplifted above 350km with a peak frequency of 7MHz, and the intensity of Ne profiles in the northern hemisphere was significant stronger than that over dip-equator and southern hemisphere (GU513 and LM42B), which agreed well with the hemispheric asymmetric structure of plasma irregularities reported by [Astafyeva *et al*., 2020].

The enhanced plasma was also detected by the radars located at the American sector. It should be noted that the blank areas over PQ052, GU513, MHJ45, WP937, JI91J signify the ionosondes failed to receive the HF echoes. It is found that the storm-enhanced plasma irregularities were observed in both of the main and recovery phase, Figure 5(h) had enough vertical profiles to describe the pattern. Also, this storm uplifted the peak height of ionosphere, but in the dawn-forenoon (it's around the midnight for local time). The largest intensity of plasma irregularities was detected over the dip-equatorial radar JI91J with a peak frequency of 7MHz, and the ionospheric peak height was uplifted about 50-80km. Compared to the Asian-Australian sector, the hemispheric asymmetric structure was not significant. Finally, the detecting results of radars in low-middle latitudes manifested that the positive plasma irregularities primary accumulated between the altitudes of 200 to 300km. Finally, the radar PQ052 near the Arctic detected an interesting result, see the red arrow in Figure 5(a). During the recovery phase, significant positive plasma irregularities at the altitudes of 110 to 150km were observed near noon, DOY 239 (August 27). The different altitudinal behaviors of plasma irregularities indicated that significant positive plasma irregularities may be triggered only in the bottom-side of auroral ionosphere, rather than in the equatorial and mid-latitude ionosphere.

Due to the TEC maps and ionosondes fail to reveal the altitudinal structures of plasma irregularities, hence the plasma densities during DOY 235-240, 2018 are simulated by the TIE-GCM for solving this problem. The averaged plasma during DOY 235-236 are selected as background value, and the altitudinal changing percent of storm-induced plasma irregularities compared to background value is shown in Figure 6. Figure 6(a)-6(f) express the temporal variations of storm-induced plasma as a function of geographic latitude at the layers span from

150 to 500km along the meridian 110°, and the vertical scale is proportional to the changing percent, which is represented by a color bar for better understand the storm-enhanced plasma behaviors.

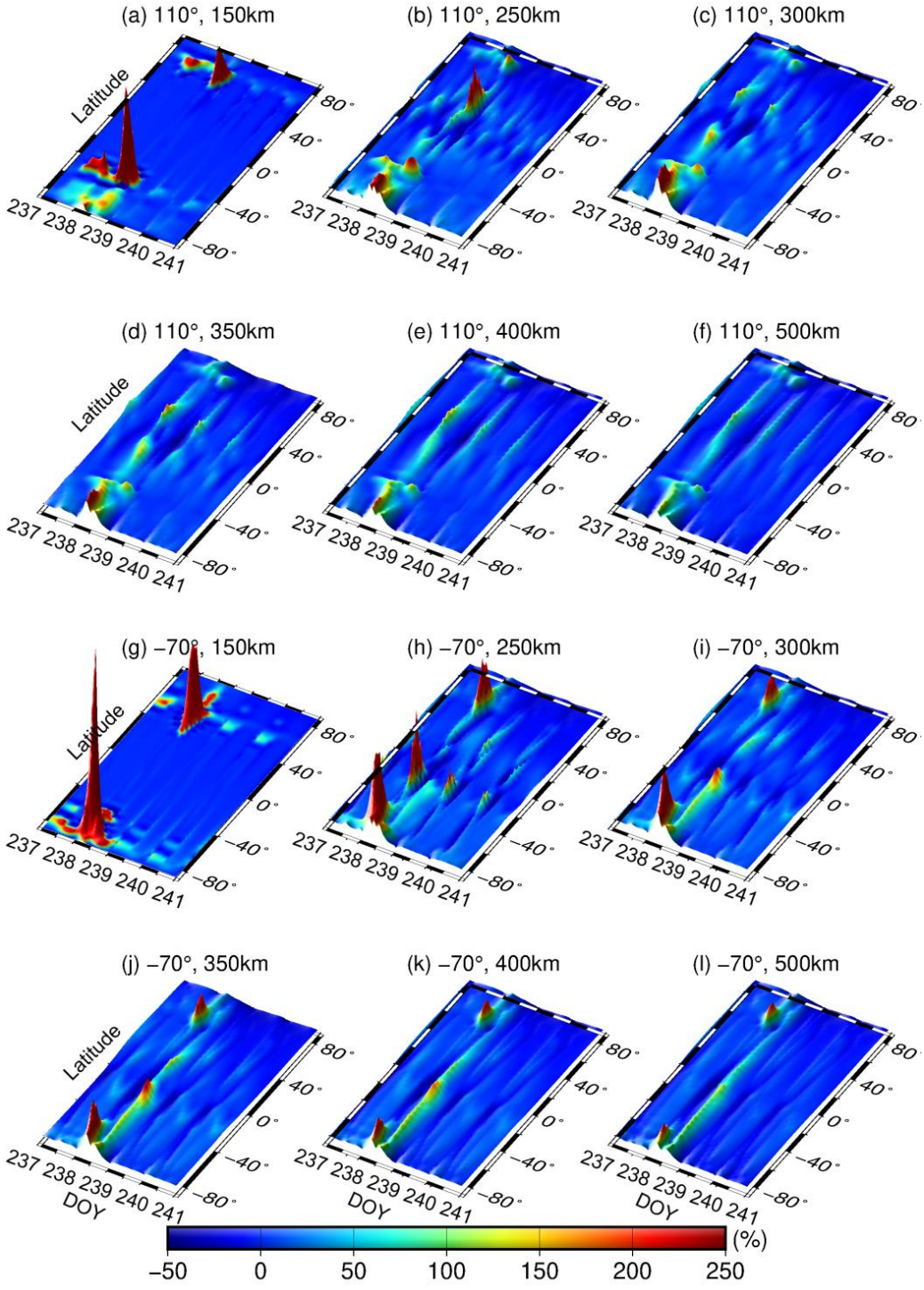

Figure 6. Ionospheric plasma disturbances at the layers span from 150 to 500km along the meridians 110° (a-f) and -70° (g-l) during day of year (DOY) 237-240, 2018

Figure 6 successes to simulate the development of double crests of the EIA at the altitudes of 150 to 500km. At the layer of 150km, since the main phase on DOY 237, two plasma increments appeared in 60°-65°N and 40°-45°S geographic latitudes along the meridian 110°, respectively. On the next day, the amplitude of plasma enhancements enhanced to 250%. At the same time, some tiny increments also occurred in the Antarctic. In the 250 km layer, the two plasma crests that located in 60°-65°N and 40°-45°S latitudes were weakened, while the plasma densities in the Antarctic were enhanced. With the increasing altitude, the plasma increments had an equatorward movement. For example, at the layer of 250 km, a plasma enhancement with a percent of ~200% appeared in 30°-40°N latitude, and a weaker increment located in 40°S latitude. The two low latitudinal enhancements moved equatorward within ±20° latitude at 350km layer. Above 350km, the two plasma crests merged into one unit and the EIA phenomena disappeared.

The change of ionospheric plasma along the meridian -70° agreed well with that over the Asian-Australian sector. Figure 6(g) shows two plasma increments appeared in 50°-60°N and 60°-70°S latitude at 150km layer, and the maximum percent exceeded 250%. The EIA phenomenon was also observed within the layers of 250 to 350km, and the crests of the EIA enhanced about 200% in DOY 238. Compared to the Asian-Australian sector, the storm-induced plasma irregularities over the American sector were larger.

3.3 Global ROTI in the main and recovery phase

The results of Figure 3-5 reveal hemispheric asymmetric structures of plasma irregularities over two sectors in different phases. In order to further investigate the development of global storm-induced ionospheric irregularities, the Rate of total electron content Index change (ROTI) that expresses sharpness of the GNSS phase fluctuations caused by ionospheric irregularities and by strong spatial gradients of TEC is estimated by the ground-based receivers. Figure 7 presents an overview of global GNSS ROTI maps during the main phase, and the time resolution of GNSS ROTI maps is one minute. The large positive and negative ROTI magnitudes are marked by red and blue, respectively; correspondingly, the small ROTI magnitudes are marked by yellow and cyan, respectively. At UT10, August 25, the ROTI map shows a low intensity of global ionospheric irregularities with an averaged value between -0.02

to 0.02TECU/min. From UT12, 25 August, the global ionospheric regularities abruptly intensified. The positive plasma irregularities primary occurred in the sunlit sector, and the magnitude of plasma irregularities over the Eastern Coast region of US and Mexico was largest with a value of 0.06TECU/min. The plasma over the nighttime Greenland was also enhanced about 0.02TECU/min.

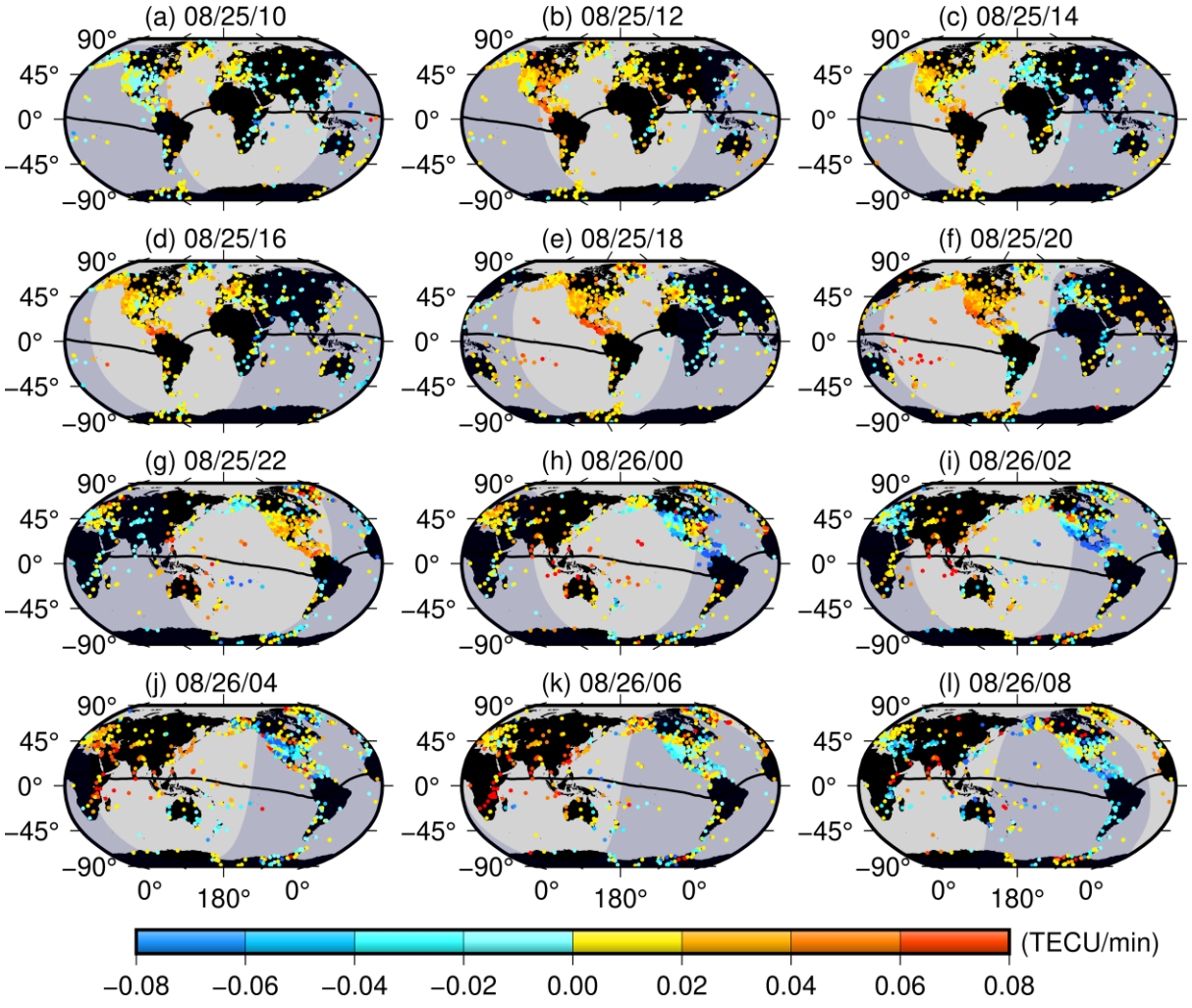

Figure 7. Global Navigation Satellite System Rate of total electron content (TEC) Index change (ROTI) maps in the main phase (mm/dd/hh) of the geomagnetic storm. The black line signifies the magnetic equator, and the shaded area shows nighttime.

After ~UT18, 25 August, the AE index rapidly increased above 500nT, even reached to a peak of 1500 to 200nT in the main phase. Correspondingly, the daytime plasma irregularities suddenly enhanced from UT18, 25 August, and significant hemispheric asymmetry of plasma irregularities was observed in the American sector. Figure 7(e) shows the equatorial and auroral plasma irregularities over the North America enhanced with a maximum magnitude of

0.08TECU/min, as well as the intensified mid-latitude plasma with a lower magnitude of 0.06TECU/min. A narrow channel of positive ionospheric irregularities was registered along the western coast of North America in the northwestward direction, the latitudinal extent of EPBs reached to 20-25°N with a maximum value of 0.1TECU/min。In addition, the GNSS ROTI observations over some ground-based receivers located at several islands in the Pacific Ocean revealed an occurrence of positive storm-induced EPBs over 160°-140°W longitudinal span, the positive ionospheric irregularities were observed at both sides of the magnetic equator and their latitudinal extent was up to 25°- 27°N/S. The feature of equatorial ionospheric ROTI agreed well with the results reported by [Cherniak and Zakharenkova, 2022]. In the nighttime hemisphere, the ionospheric irregularities were negative with a low intensity. From 26 August, the GNSS ROTI over the Western Coast of The North America and Greenland turned negative, though some negative irregularities were under sunlit sector. However, the ROTI over the European-African sector gradually turned positive and enhanced to a largest magnitude during UT04-06, 26 August. The positive irregularities with a maximum value of 0.1TECU/min were observed in Europe, Africa and Asia, rather than Australia, though it was also under the sunlit sector. The results conclude that the hemispheric asymmetry of plasma irregularities was also significant during the ending of the main phase, which expresses the ROTI over Africa was larger than that over Europe, while it was opposite in the Asian-Australian sector.

Figure 8 shows an overview of global ionospheric irregularities during the recovery phase of the geomagnetic storm, it is found that the storm also induced strong GNSS ROTI, especially over the American sector. At UT10, 26 August, strong plasma irregularities with a level of 0.06TECU/min appeared over the South America, as well as the equator and mid-high latitudes of the North America. In addition, it is interesting that a narrow channel of positive ionospheric irregularities was observed in the northwestward direction over the nighttime Alaska. Two hours later, a significant hemispheric asymmetry of plasma irregularities developed over the American sector, which expresses the storm-induced plasma over 20°S to 45°S latitudinal span enhanced larger than 0.08TECU/min, while the GNSS ROTI over the North America kept in a low level of 0.02 to 0.04TECU/min. Except the American sector, the plasma irregularities over other daytime or nighttime Continents maintained in a low level. From UT14, 26 August, the hemispheric asymmetry was reversed, which means high-

magnitude GNSS ROTI concentrated in the North America. Here, the signatures of the ionospheric irregularities persisted for many hours till the midnight. Furthermore, significant equatorial and mid-latitude positive plasma irregularities also appeared in the daytime Asian-Australian and European-African sectors, as see Figure 8(g) and 8(j). In the following hours, the global GNSS ROTI gradually recovered to a low level.

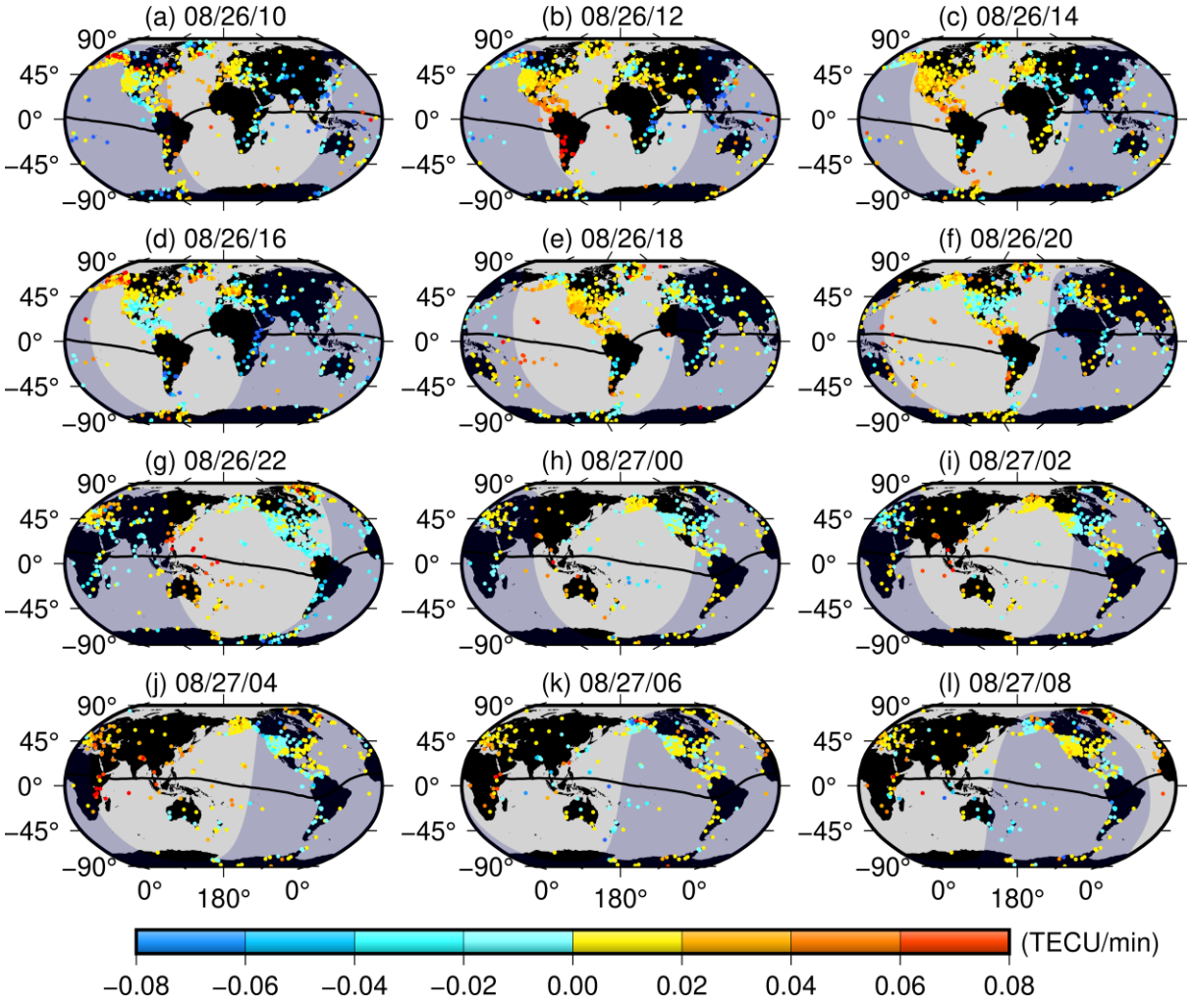

Figure 8. Similar to Figure 7, but in the recovery phase

3.4 Potential physical-chemical drivers of ionospheric irregularities

3.4.1 Potential drivers of equatorial and mid-latitude ionospheric irregularities

Thermospheric composition change is an important driver in inducing positive or negative ionospheric irregularities. Therefore, the thermospheric density ratio O/N_2 measured by GUVI on board the space-borne TIMED satellite (~625km) is analyzed. It is noted that the density ratio O/N_2 is a height integrated quantity within the orbit altitudes of the GNSS constellation

and the GUVI satellite. At the same time, the global topside TECs derived from Swarm-A and Swarm-B are also investigated, and the TEC signifies the integrated electrons within the altitudes from the orbit of Swarm microsatellite to the orbit of GNSS constellation. Figure 9 give an overview of daily topside TEC and O/N_2 during the storm. One can also notice that the TEC distribution is slightly different in the data of two satellites, which is most likely due to the ~80km of difference in altitude. Both the profiles of Swarm-A and Swarm-B conclude that the topside TECs over the Asian-Australian and American sectors were quiet before UT12, 25 August, the averaged TEC was under 6TECU. Figure 9(b) shows the TEC profile over the American sector suddenly enhanced, and the expanded profiles covered the eastern Pacific, this phenomenon was also validated by the observation of Swarm-B. During UT00-12, 26 August, the TEC over the Asia-Australia sector strengthened remarkably with a maximum value of exceeded 12TECU. After that, the enhanced TEC profiles gradually decreased and recovered to a normal level. The profiles derived from Swarm-B agreed well with that of Swarm-A that large-scale positive TEC irregularities appeared over the Asian-Australian and American sectors.

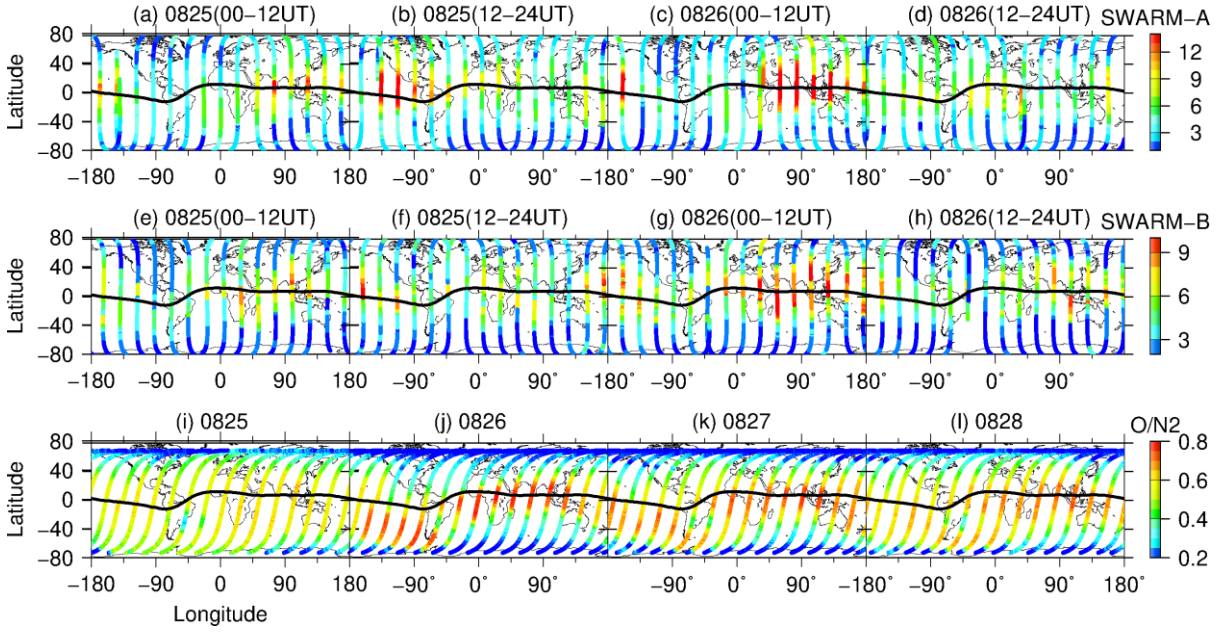

Figure 9. Topside TEC variations measured by GPS receivers on board the (a) – (d) Swarm-A and (e) – (h) Swarm-B on 25-26 August, (i) – (l) thermospheric density ratio O/N_2 as measured by the GUVI satellite during August 25-28. The black thin curve signifies the magnetic dip equator.

Figure 9(i) shows the density ratio O/N_2 was inversely proportional to geographic latitude, the O/N_2 ranged from 0.3 to 0.6 in quiet days. However, the O/N_2 ratio had a suddenly change with the eruption of a storm. Specifically, the O/N_2 in low-middle latitudes increased remarkably with a maximum value of 0.8, while the O/N_2 in Polar regions decreased to 0.2. Besides, the enhanced O/N_2 had a southward excursion in the America sector. For example, see panel 9(j), the O/N_2 in North America was about 0.4, while this ratio increased to 0.8 in South America. In the following two days, the storm-effect O/N_2 gradually decreased with the geomagnetic field recovered to a normal level. The change of density ratio O/N_2 agreed well with the TEC irregularities, which implied the change of density ratio O/N_2 may be an important driver in generating plasma disturbances. O/N_2 has a good positive correlation with plasma density, and it has proven to be a successful indicator of a neutral composition disturbance for analyzing ionospheric storms [*Strickland et al.*, 2001]. The ionospheric ion density loss rate is proportional to the molecular concentration, an increment of the mean molecular mass causes a decrement in electron density, while a decrement of molecular concentration provokes a positive disturbance.

As we know, at the altitudes of 90 to 130 km, many electrons move westward driven by dayside electric field. According to the equatorial dynamo effect, the westward electron flow generates a dayside eastward electric current, the electric current is defined as equatorial electrojet (EEJ). The EEJ could be changed severely suffered from the disturbed electric field penetrated from magnetosphere under a strong geomagnetic storm. The EEJ signatures can be estimated by taking the difference between the horizontal components performed by a pair of off-the-equator and at-the-equator magnetometers. The horizontal components of the magnetometers PHU, DLT, SJG and HUA located at the Asian-Australian and American sectors are used to investigate the storm-effect EEJ changes, and the observations of magnetometers are obtained from the International Real-time Magnetic Observatory Network (https://intermagnet.org/index-eng.php).

Figure 10(a) and 10(b) show the changes of EEJ signatures along with the Dst index over the Asian-Australian and American sectors. It is found that the Dst abruptly decreased with a geomagnetic storm erupted on UT14, 25 August 25 2018, as well as the horizontal components of the magnetometers PHU, DLT, SJG and HUA. In Figure 10(a), the equatorial magnetometer GUA decreased to a minimum value of ~-270nT during UT 06-08, 26 August, and the

differential component between GUA and KAK had a negative perturbation with a minimum value of -100nT. Correspondingly, the TEC over the station PIMO enhanced 18TECU in the severest moment. The EEJ changes estimated by the difference between HUA and KOU in Figure 10(b) agreed well with that over the Asian-Australian sector. The EEJ signature had two distinct perturbations in the afternoons of 26-27 August with an amplitude of ~50nT. The differential TEC over station UNSA was consistent with the EEJ signature. Two TEC enhancements appeared in the recovery phase of geomagnetic storms, the maximum delta TEC reached to 14TECU. The results demonstrate that the change of EEJ may be an important driver in triggering storm-effect TEC disturbances. However, the slight EEJ fluctuations cannot fully responsible for the strong TEC enhancements. Therefore, more drivers should be analyzed for explaining the remarkable ionospheric disturbances.

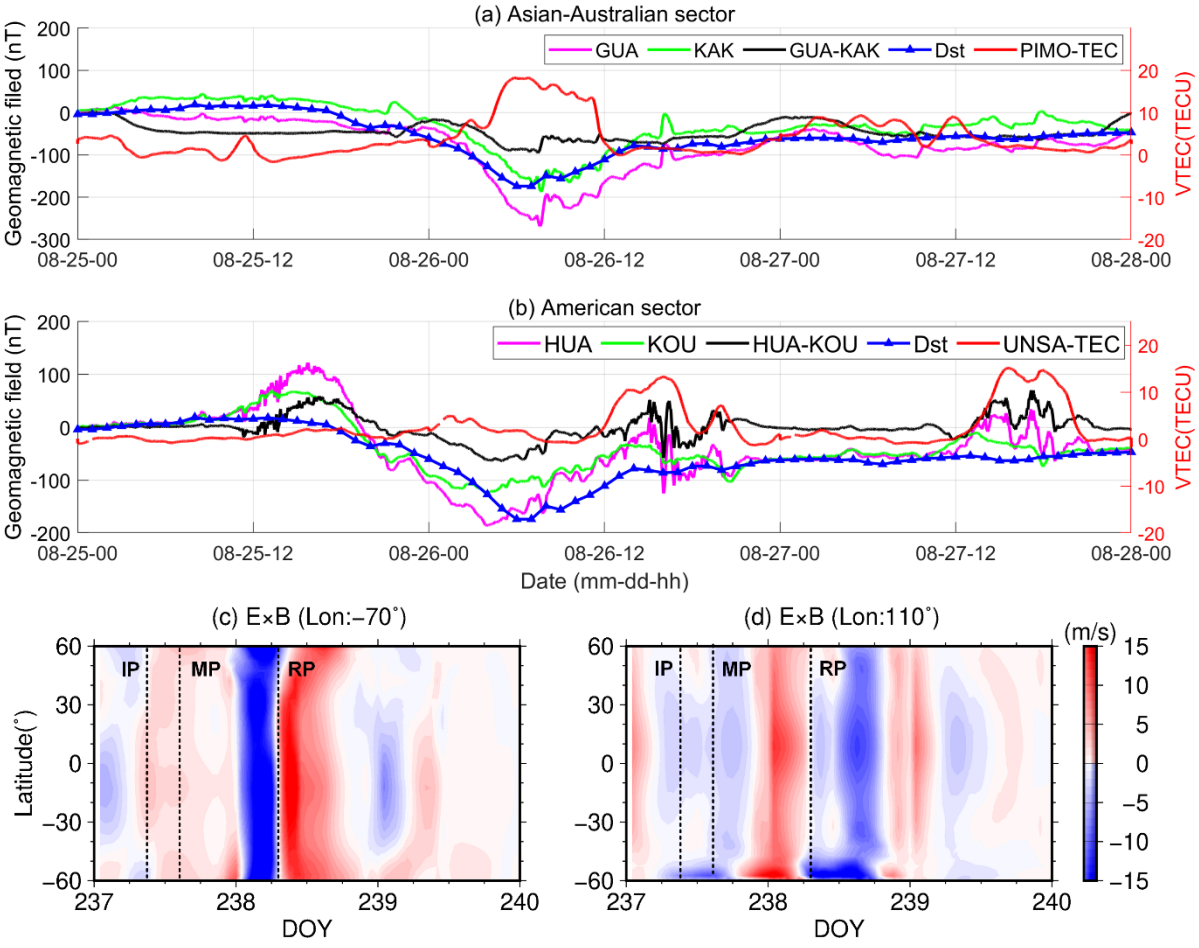

Figure 10. Variations of the horizontal intensity of the geomagnetic field, equatorial electrojet (EEJ), differential TECs and Dst value in the Asian-Australian (a) and American (b) sectors, as well as the differential latitudinal vertical E×B drifts along the -70° (c) and 110° (d) longitudes.

The equatorial plasma fountain effect plays a dominating role in generating the EIA. The vertical E×B drift drives the equatorial plasmas upward to higher altitudes, and the accumulated plasmas diffuse down to higher latitudes along the geomagnetic field lines, which results two high concentrated plasma crests distributed on both sides of the magnetic equator [*Balan and Bailey*, 1995; *Li et al.*, 2021]. In the fountain process, a stronger E×B drift could lift more plasmas to higher altitudes, and the crests of EIA generated by the plasma diffused process are stronger and more poleward. Therefore, the changes of vertical E×B drift may be another driver for the equatorial and mid-latitude plasma perturbations. The latitudinal changes of vertical E ×B drifts along the -70° and110° longitudes are simulated by the TIE-GCM in Figure 10(c) and 10(d). Figure 10(c) expresses the E×B drifts along the meridian -70° began to increase from UT14, 25 August, the slight E×B enhancement was 3 to 5m/s. Then the nighttime E×B drifts suddenly weakened with a maximum decrement of -15m/s in the dawn, 26 August (LT, it was at night). Subsequently, the daytime differential E×B drifts turned positive from UT8, 26 August with a maximum increment of 15m/s. In the forenoon, 27 August (DOY 239), the differential E×B had a hemispheric asymmetric structure, which expressed that the differential E×B on DOY 239 enhanced ~5m/s in the southern hemisphere. In the Asian-Australian sector, the E×B drift enhanced from UT20, 25 August with a magnitude of 5 to 10m/s (LT, it was in daytime). In the following day, a slight positive E×B irregularity was also observed.

The results in Figure 9-10 reveal that the thermospheric density ratio O/N_2, equatorial electrojet and vertical E×B drift were suffered from the strong geomagnetic storm seriously. Among them, the equatorial electrojet was activated by the disturbed electric field penetrated from magnetosphere, and the changes of vertical E×B drifts may be associated with PPEFs and DDEFs. Therefore, it is believed that the equatorial and mid-latitude ionospheric irregularities are a combined action of multiple physical-chemical processes. The enhanced density ratio O/N_2, vertical E×B drift and equatorial electrojet played a decisive role in inducing the positive irregularities. In the recovery phase, the hemispheric asymmetric O/N_2 and E×B drift on August 27 may be responsible for the asymmetric TEC over the American sector in Figure 3.

3.4.2 Potential drivers of Auroral ionospheric irregularities

The GNSS ROTI, sounder density profiles and TIE-GCM's simulations demonstrate significant Auroral ionospheric irregularities induced by the storm. For further to reveal the vertical structures of Auroral ionospheric irregularities, the plasma irregularities within the

altitude of 96 to 400km along the -70°, 0° and 110° longitudes are simulated by the TIE-GCM. Figure 11(a) - 11(c) show the temporal variations of differential plasma density as a function of altitude. In Figure 6, the TIE-GCM's simulation find that at the layer of 150km, largest plasma irregularities with a changing percent of >250% located in the 70°S – 80°S latitude span. Therefore, the geographic latitude is selected as 77.5°S in Figure 11(a) – 11(c). It should be noted that the vertical scale of each panel is similar to Figure 7, but for the amplitude of plasma irregularities. We can find that significant plasma enhancements occurred in topside and bottom-side of the Antarctic ionosphere along three longitudes. In the main phase, the increment along the meridian -70° was maximum with a value up to 6×10^5el/cm^3, followed by the meridian 0°, the last was the weakest increment of 4×10^5el/cm^3 along the meridian 110°. In addition, the plasma fluctuations were also observed in bottom-side ionosphere along the meridians -70° and 0°, except the meridian 110°.

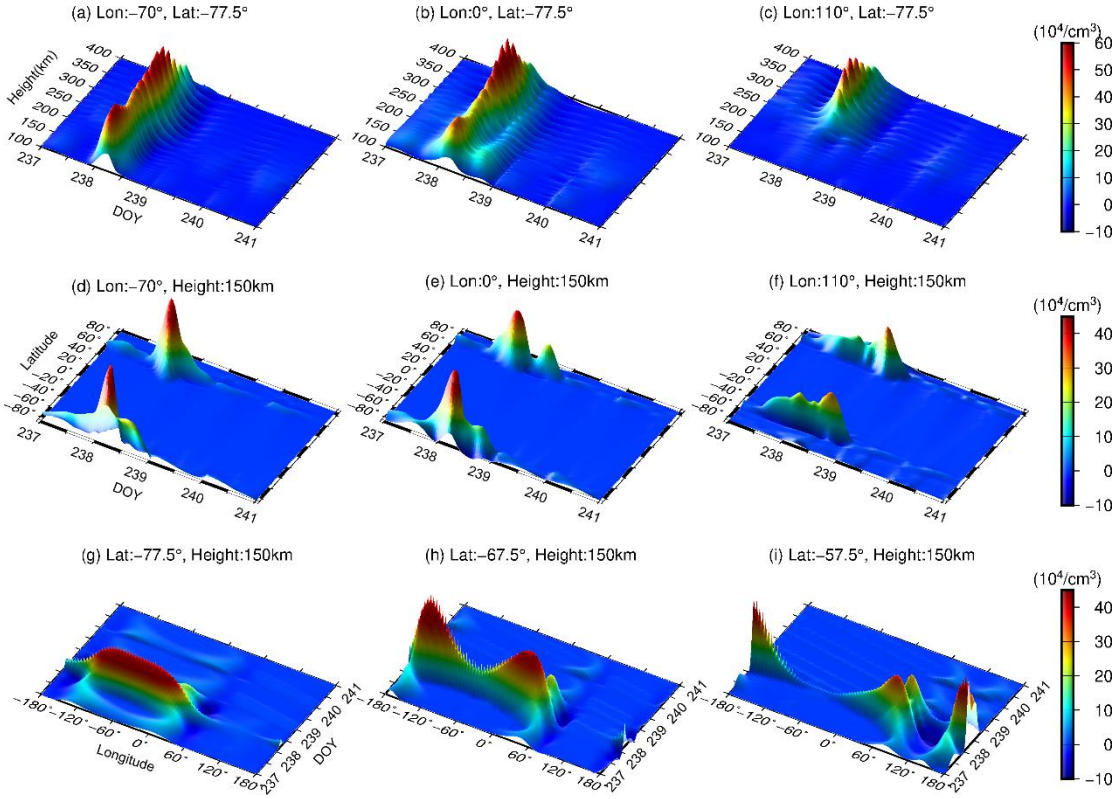

Figure 11. Structures of differential plasma irregularities along the -70°, 0° and 110° longitudes as a function of height (a-c), geographic latitude (d-f), and geographic longitude (g-i) during DOY 237 – 240.

Did the geomagnetic storm only disturb the bottom-side ionosphere in the western Antarctic? To address the question, the temporal variations of differential bottom-side plasma

(150km) as a function of geographic latitude along the meridians -70°, 0° and 110° are shown in panels 11(d) - 11(f). It is found that significant storm-effect plasma increments occurred in bottom-side ionosphere over all three longitudinal sectors, but the geographic latitudes of plasma increments were not stationary. Panel 11(d) shows two plasma crests were located in 60°N and 80°S latitudes, respectively. The two crests had a northward movement in Eastern hemisphere. For example, in the Asian-Australian sector, the plasma crests moved to 80°N and 60°S latitudes with a weaker value of 3×10^5el/cm^3. The law of latitudinal motion of bottom-side plasma enhancements in different longitudinal sectors was associated with the asymmetric structure of geomagnetic field.

Figure 11(g) - 11(i) express the longitudinal structures of differential plasma (150km) as a function of day of year (DOY), the geographic latitudes in three sectors are 77.5°S, 67.5°S, 57.5°S, respectively. Panel 11(g) reveals positive plasma irregularities occurred in -120° ~ 0° longitudinal span on 26 August with a value of 4×10^5el/cm^3. Along the 67.5°S latitude, the plasma irregularities had a double-peak structure that occurred in -180° ~ 60° longitudinal span. Along the 57.5°S latitude, the double-peak plasma increments were observed in 0° ~ 90° and 150° ~ -120° longitudinal span. Compared to Auroral plasma irregularities, the intensity of bottom-side plasma irregularities decreased in middle geographic latitude. The results conclude that the strong storm not only induced topside plasma fluctuations, but also triggered positive bottom-side plasma irregularities near the Auroral zone (~ > 50°N/S), which is consistent with the sounder profiles of the radar PQ052 in Figure 5(a).

In order to explain the development of Auroral ionospheric irregularities, the Joule heating, O^+ and O_2^+ ion densities within the altitudes of 100 to 400 km are simulated by the TIE-GCM. In addition, the neutral mass density decreases exponentially with height, and the Joule heating per unit mass at higher altitude is much larger than that at the lower altitude. The bottom-side change will be neglected if only focus on the differential Joule heating per unit mass, thus the ratio of the changed Joule heating during storms compared to the quiet background values is also investigated. In the Arctic, the study area is selected at 110°E, 67.5°N. The vertical changes of Joule heating, ratio of enhanced Joule heating, O^+ and O_2^+ ion density over the Arctic are shown in Figure 12(a) - 12(d). It is found that the Joule heating enhanced from the main phase with a magnitude of 1×10^4erg/g/s, then the enhanced Joule heating reached a maximum in the

recovery phase with a value of 3×10^4erg/g/s. After that, the Joule heating gradually recovered to backgrounds.

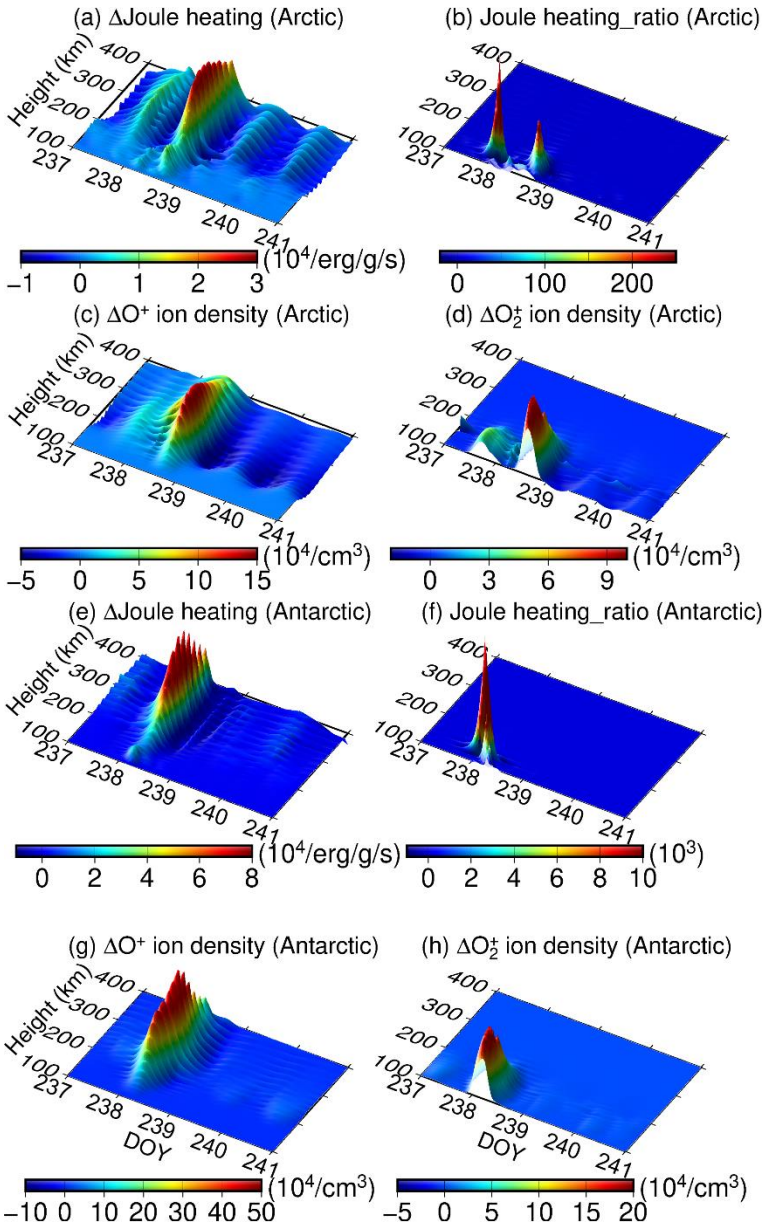

Figure 12. Vertical changes of Joule heating, ratio of enhanced Joule heating, O^+ and O_2^+ ion density over the locations (110°E, 67.5°N, (a)-(d)) and (70°W, 77.5°S, (e)-(h)) during DOY237-240

Similar to the variation of topside Joule heating, the positive Joule heating disturbance was also observed under 200km on DOY237-238 with a slight value of 1×10^4erg/g/s. Different from the absolute change of the differential Joule heating in Figure 12(a), Figure 12(b) shows the Joule heating in the main and recovery phases enhanced more 200 times than the background values, and the maximum Joule heating enhancements were located in the altitudes

of 100-150km. The changes of O^+ ion density in panel 12(c) agreed well with the Joule heating, the O^+ ion density enhanced from DOY237 and grew stronger on DOY238 above the 200 km layer, the maximum value reached to $1.5\times10^5/cm^3$. An O_2^+ increment generated from UT14, DOY237, and grew to $1\times10^5 el/cm^3$ on DOY238. Different from O^+ ion, the O_2^+ increments were mainly occurred under the 200 km layer, which is consistent with the behaviors of bottom-side enhanced Joule heating in Figure 12(b).

In the Antarctic, the study area is selected at 70°W, 77.5°S. The changes of Joule heating over the Antarctic agreed well that over the Arctic, but the positive Joule heating disturbances only appeared in the main phase, which is consistent with the variation of storm-effect Antarctic ionospheric plasma in Figure 11(a). The magnitude of enhanced Joule heating over the Antarctic was several times larger than that over the Arctic. Figure 12(e) expresses the topside and bottom-side Joule heating enhanced about $8\times10^4 erg/g/s$ and $2\times10^4 erg/g/s$, respectively. However, Figure 12(f) indicates that the changed ratio of bottom-side Joule heating in the main phase was larger than that in the topside significantly, and the maximum enhanced ratio exceed 1×10^4. Similar to Figure 12(c) - 12(d), in the main phase, the O^+ ion density over the Antarctic enhanced about $5\times10^5/cm^3$ above the 200km layer, and the bottom-side O_2^+ ion density enhanced about $2\times10^5 el/cm^3$.

The changed amplitudes of Joule heating, O^+ and O_2^+ ion density over the Antarctic were much stronger than that over the Arctic, which agrees well with the magnitude of Polar ionospheric plasma disturbance in Figure 11. During a space weather event, the sudden enhanced energy could ionize the main neutral gases O_2 and N_2 that leads to an increment in ion density [*Gordon et al.*, 2020]. Our simulations confirmed the theory that the enhanced Joule heating could accelerate the Polar ionospheric ionization process, and the enhanced O^+ and O_2^+ ion densities are responsible for the topside and bottom-side plasma increments, respectively.

Geomagnetic storms not only form storm-enhanced densities (SEDs) in low-middle latitudes and tongues-of-ionization at the polar cap, but also change the global magnetic field and strength ionospheric-magnetospheric current systems [*Walach et al.*, 2021]. Ionosphere is a conductor, and the Polar ionosphere contains significant electric fields. The electric fields could drive the ionospheric current that close field-aligned currents flowing in the ionospheric-magnetospheric system, generate Joule heating in the upper atmosphere, and even control the

circulation of ionospheric plasma that change the Polar ionospheric electron density structure. The ionospheric electric potential contour maps calculated with the Super Dual Auroral Radar Network (SuperDRAN) Assimilative Mapping procedure (http://vt.superdarn.org/tiki-index.php?page=ASCIIData) are used for investigating the spatial-temporal variations of the Polar convection patterns in the main phase of the geomagnetic storm.

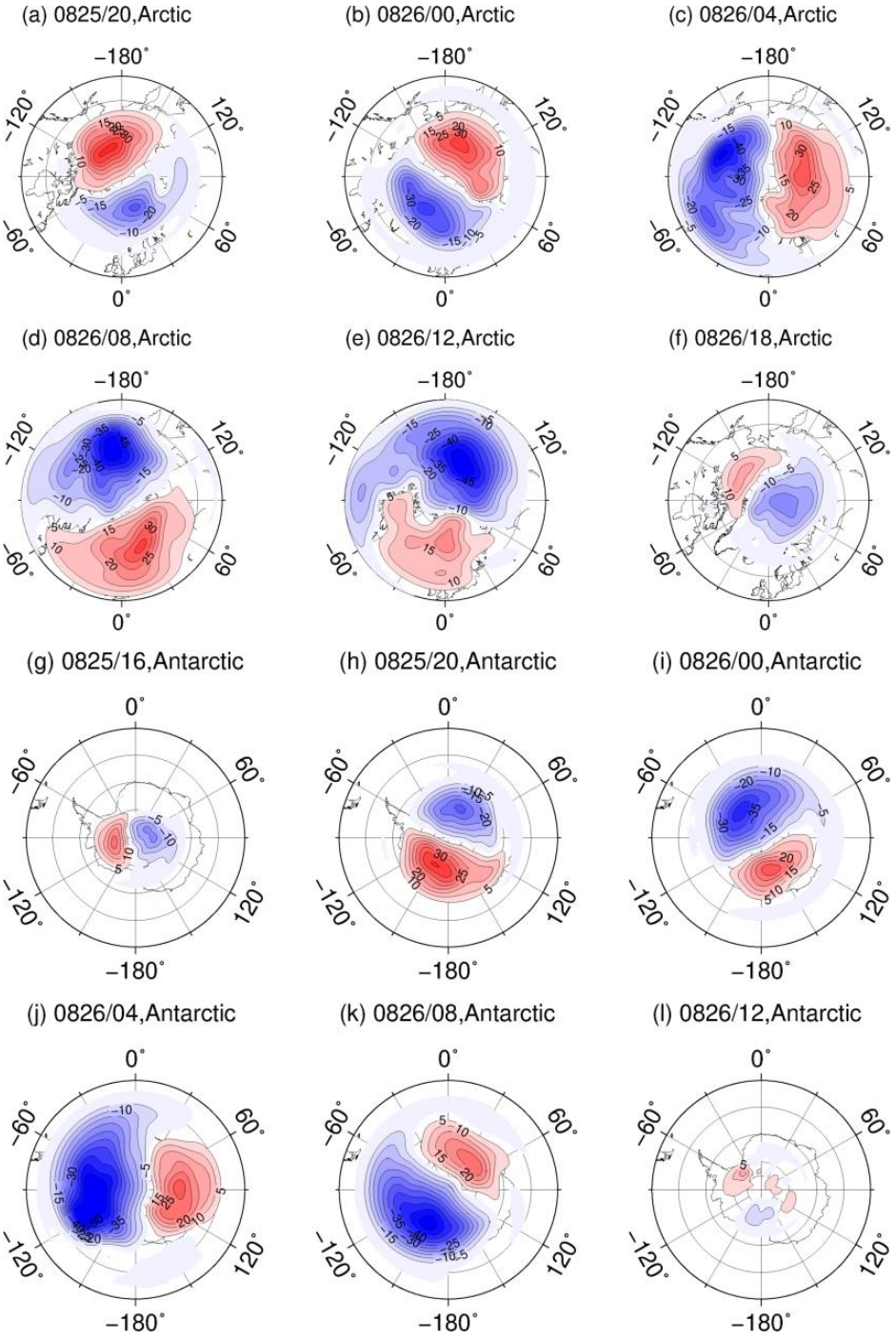

Figure 13. Maps of the electric potentials from SuperDARN over the Arctic (a-f) and Antarctic (g-l) during August 25-26, 2018, the red and blue contours signify positive and negative potentials, respectively.

As shown in Figure 13, the positive and negative ionospheric electric potentials are indicated by red and blue contours. Usually the potential pattern has a maximum near dawn and a minimum near dusk. The difference between the maximum and minimum of potential is called the cross polar voltage. Figure 13(a) - f(f) gives an overview of the spatial-temporal evolution of electric potentials over the Arctic from UT20, 25 August to UT18, 26 August. At UT20, 25 August, a positive electric potential with a maximum value of 41kv distributed in -90° ~ -180° longitudinal span, and the negative electric potential with a minimum magnitude of -32kv occurred in -60° ~ 120° longitudinal span. From 26 August, the Polar electric potential intensified remarkably with the decreasing Dst index. The strongest electric potential occurred in UT04-08, 26 August, concurrently with the AE index reached to a peak of 1500 to 2000nT. For example, the negative potential in Figure 13(d) dropped to -53kv, on the contrary, the positive potential enhanced to 36kv, and the cross polar voltage reached to 89kv. One can see that during the ending of the main phase, the convection zone in the Arctic extended ~ 50°N, the scope of enhanced convection zone was consistent with the geographic latitude of radar PQ052 (Figure 2(a)) that was the station with a minimum latitude could detect the bottom-side ionospheric regularities. Similar to the Arctic electric potential, the scale and scope of electric potential over the Antarctica also enhanced and expanded remarkably. The negative potential dropped from -32kv at UT20, 25 August to -61kv at UT04, 26 August, while the corresponding positive potential reduced from 40kv to 33kv, the maximum cross polar voltage at the UT04, 26 August reached to 94kv. The scale of Antarctic storm-effect electric potential was stronger than that over the Arctic, but the scope was smaller.

During active space weather events, the sudden energy and momentum deposited in the high-latitude ionosphere and thermosphere, mostly in the forms of particle precipitation and Joule heating. The incident precipitating particles gradually transfer energy to the different layers of the ionosphere, and ionize more charged particles as the stronger deposited energy. The accelerated ionization process enhances the ionospheric current flowing in the medium. The particle precipitation and Joule heating control the variations of the short-scale structures of the ionosphere-thermosphere, which results in an increment in the electric conductivity and heating of the ionosphere-thermosphere system. During the April 5, 2010 geomagnetic storm, the TIE-GCM simulations concluded that additional particle precipitation not only largely

increases ionospheric conductivity, but also causes remarkable Joule heating enhancements[*Sheng et al.*, 2017]. The enhanced conductivity, electric field, and a combination of both could intensify the ionospheric electric currents. The current density is proportional to the ionospheric conductivity directly, and the ionospheric conductivity is proportional to the plasma density directly [*Cherniak and Zakharenkova*, 2018]. Therefore, there is a close connection between magnetosphere energy deposition, particle precipitation, ionospheric currents intensification, Joule heating, and SEDs generation. Figure 12 - 13 reveal the plasma density, Joule heating and ionospheric electric potential affected by the storm all enhanced significantly, which further confirms the charged particles diffusion process reported by previous literatures. Thus, it is believed that the storm-induced Polar plasma irregularities are associated with the additional energy input through the ways of particle precipitation, Joule heating and ionospheric currents intensification.

4. Conclusion

The 25-27 August geomagnetic storm was a surprising space event that generated in the background of very low solar activity. The prominent features of global ionospheric response to the strong geomagnetic storm that occurred at low solar activities are analyzed by ground-based instruments (GNSS receivers and ionosondes) and space-borne constellation (Swarm). This geomagnetic triggered several unusual ionospheric plasma irregularities depend on geographic longitude, latitude and altitude, and the potential drivers for explaining these irregularities are also discussed using the observations of magnetometers, GUVI profiles and TIE-GCM's simulations. Some important conclusions are drawn as follows:

(1) In the Asian-Australian sector, the observations of global GNSS receivers find that the storm enhanced the equatorial and mid-latitude TEC to a maximum value of 40TECU in the ending of main phase and the beginning of recovery phase. While in the American sector, this storm triggered a remarkable TEC hemispheric asymmetry in the recovery phase, which expresses TEC depletion occurred in North America, and low-level TEC enhancements occurred in mid-latitudes of South America. In the following two days, the equatorial and mid-latitude TEC over the American sector significant enhanced ~10TECU. The phenomenon was also validated by the ionospheric topside profiles derived from the Swarm-A, the space-borne

observations not only confirmed the plasma density enhancements over the Asian-Australian and American sectors that happened in the main and recovery phases, respectively, but also detected an enhanced double-peak crests of EIA that caused by a daytime "superfountain" effect that driven by the PPEFs.

(2) The sounder profiles of ionosondes found that the storm induced positive plasma irregularities in equatorial and mid-latitude ionosphere, and the enhanced plasma irregularities primary accumulated in altitudes of 200 to 300km with a maximum frequency of 7MHz. Different from TEC's change, a hemispheric asymmetric structure of ionospheric vertical frequency was observed in the Asian-Australian sector, which expresses the topside (> 300km) plasma over the ionosonde IC437 located in northern hemisphere increased a maximum frequency of 7MHz. In addition, the profiles of the ionosonde PQ052 near the Arctic zone revealed an interesting finding, that is the storm could trigger positive plasma irregularities in the bottom-side (<150km) ionosphere near Auroral zone. Furthermore, the TIE-GCM succeeded to simulate the temporal variation of differential plasma density as a function of geographic latitude in the altitudes of 150 to 500km. The simulation not only discovered positive plasma irregularities with a ratio of > 250% at the layer of 150km, but also captured the development of the double crests of EIA in the altitudes of 250 to 400km.

(3) This study first time to give an overview of the development of global ROTI in the whole phase. The global ROTI maps found remarkable hemispheric asymmetry of plasma irregularities in a particular time. In the beginning of the main phase (UT12 – 22, 25 August), the ROTI in the American sector had a hemispheric asymmetric structure, which expressed the plasma irregularities in North America were larger than that in South America, the maximum irregularities appeared in Auroral zone and a narrow channel along the western coast of North America with a value of 0.1TECU/min. In the ending of the main phase, the plasma irregularities over Africa were larger than that in Europe, while it was opposite in the Asian-Australian sector. In the recovery phase, the GNSS receivers not only detected large plasma irregularities in nighttime Alaska, but also found a new hemispheric asymmetry in the American sector, which expressed the mid-latitude plasma with a positive ROTI of 0.08TECU/min in South America was significantly larger than that in North America. The latitudinal plasma irregularities agreed well with TEC enhancements.

(4) The GUVI profiles indicated that the storm also induced significant thermospheric composition change during 26-27 August, which expressed positive density ratio O/N_2 change occurred in equatorial ionosphere, and negative change appeared in Auroral zone. A hemispheric asymmetry of enhanced density ratio O/N_2 was observed in South America. In addition, the EEJ were suffered from the enhanced equatorial electric field caused by geomagnetic storm slightly. The observations of magnetosphere demonstrated slight positive EEJ fluctuations occurred in the Asian-Australian and American sectors. Furthermore, the simulations of TIE-GCM concluded that the daytime E×B drifts enhanced exceeded 15m/s in two sectors on 25-26 August. The enhanced E×B drifts reinforced the equatorial fountain effect and strengthen the ionospheric double-peak structure at the layers of 250 to 350 km. The equatorial and mid-latitude plasma irregularities are believed to be a combined action of thermospheric composition change, equatorial electrojet, vertical E×B drifts.

(5) The simulations of TIE-GCM demonstrated that the storm not only enhanced topside ionospheric plasma density, but also triggered positive plasma irregularities in bottom-side ionosphere near Auroral zone, which agreed well the observation of ionosonde PQ052. The bottom-side plasma irregularities had a poleward excursion along the magnetic equator, which was associated with the longitudinal offset of geomagnetic field. In addition, the positive Joule heating irregularities in the altitudes of 100 to 400km were observed in both Arctic and Antarctic, and the changed ratio of bottom-side Joule heating enhanced > 250%. The temporal-spatial changes of Joule heating were consistent with the behaviors of Polar plasma irregularities. The enhanced O^+ ion density was responsible for the topside plasma irregularities, and the increment of O_2^+ ion density may be a dominating driver for the positive bottom-side plasma irregularities. Furthermore, the Polar ionospheric electric potential suffered from the storm severely, the cross polar voltage abruptly enhanced to 89kv and 94kv in the Arctic and Antarctic, respectively, and the enhanced electric potential expanded remarkably that the boundary reached to ~50°N geographic latitude. The Polar ionospheric irregularities may be associated with the additional energy input through the ways of particle precipitation, Joule heating and ionospheric currents intensification.

Acknowledgement: The authors greatly appreciate the financial support from the Natural Science Foundation of Jiangsu Province (Grant Nos. BK20200646, BK20200664), and the Fundamental Research Funds for the Central Universities (Grant No. 2020QN31).

Data Availability Statement: The author acknowledge UNAVCO for GNSS observation files (https://www.unavco.org/data/gps-gnss/gps-gnss.html), Global Ionosphere Radio Observatory for sounder profiles (jdbc:firebirdsql://didbase.giro.uml.edu/didb), European Space Agency for SWARM profiles (https://earth.esa.int/eogateway/missions/swarm/data), GSFC for solar and geomagnetic indices (https://omniweb.gsfc.nasa.gov/form/dx1.html), INTERMAGNET for geomagnetic field data (https://intermagnet.org/index-eng.php), SuperDARN for ionospheric electric potential map (http://vt.superdarn.org/tiki-index.php?page=ASCIIData), High Altitude Observatory for the TIE-GCM model (https://www.hao.ucar.edu/modeling/tgcm/tie.php).

Reference

Aa, E., W. Huang, S. Liu, A. Ridley, S. Zou, L. Shi, Y. Chen, H. Shen, T. Yuan, and J. Li (2018), Midlatitude plasma bubbles over China and adjacent areas during a magnetic storm on 8 September 2017, *Space Weather*, *16*(3), 321-331. https://doi.org/10.1002/2017SW001776

Astafyeva, E., I. Zakharenkova, and M. Förster (2015), Ionospheric response to the 2015 St. Patrick's Day storm: A global multi-instrumental overview, *Journal of Geophysical Research: Space Physics*, *120*(10), 9023-9037. https://doi.org/10.1002/2015JA021629

Astafyeva, E., M. S. Bagiya, M. Förster, and N. Nishitani (2020), Unprecedented hemispheric asymmetries during a surprise ionospheric storm: A game of drivers, *Journal of Geophysical Research: Space Physics*, *125*(3), e2019JA027261. https://doi.org/10.1029/2019JA027261

Atıcı, R., and S. Sağır (2020), Global investigation of the ionospheric irregularities during the severe geomagnetic storm on September 7–8, 2017, *Geodesy and Geodynamics*, *11*(3), 211-221. https://doi.org/10.1016/j.geog.2019.05.004

Balan, N., and G. Bailey (1995), Equatorial plasma fountain and its effects: Possibility of an additional layer, *Journal of Geophysical Research: Space Physics*, *100*(A11), 21421-21432. https://doi.org/10.1029/95JA01555

Chang, H., H. Kil, A. K. Sun, S. R. Zhang, and J. Lee (2022), Ionospheric Disturbances in Low-

752 and Midlatitudes During the Geomagnetic Storm on 26 August 2018, *Journal of*
753 *Geophysical Research: Space Physics*, *127*(2), e2021JA029879.
754 https://doi.org/10.1029/2021JA029879
755 Cherniak, I., and I. Zakharenkova (2018), Large-scale traveling ionospheric disturbances origin
756 and propagation: Case study of the December 2015 geomagnetic storm, *Space Weather*,
757 *16*(9), 1377-1395. https://doi.org/10.1029/2018SW001869
758 Cherniak, I., and I. Zakharenkova (2022), Development of the Storm-Induced Ionospheric
759 Irregularities at Equatorial and Middle Latitudes During the 25-26 August 2018
760 Geomagnetic Storm, *Space Weather*, *20*(2), e2021SW002891.
761 https://doi.org/10.1029/2021SW002891
762 Crowley, G., C. Hackert, R. Meier, D. Strickland, L. Paxton, X. Pi, A. Mannucci, A.
763 Christensen, D. Morrison, and G. Bust (2006), Global thermosphere-ionosphere response
764 to onset of 20 November 2003 magnetic storm, *Journal of Geophysical Research: Space*
765 *Physics*, *111*(A10). https://doi.org/10.1029/2005JA011518
766 de Paula, E. R., C. B. de Oliveira, R. G. Caton, P. M. Negreti, I. S. Batista, A. R. Martinon, A.
767 C. Neto, M. A. Abdu, J. F. Monico, and J. Sousasantos (2019), Ionospheric irregularity
768 behavior during the September 6–10, 2017 magnetic storm over Brazilian equatorial–low
769 latitudes, *Earth, Planets and Space*, *71*(1), 1-15. https://doi.org/10.1186/s40623-019-
770 1020-z
771 Dmitriev, A., A. Suvorova, M. Klimenko, V. Klimenko, K. Ratovsky, R. Rakhmatulin, and V.
772 Parkhomov (2017), Predictable and unpredictable ionospheric disturbances during St.
773 Patrick's Day magnetic storms of 2013 and 2015 and on 8–9 March 2008, *Journal of*
774 *Geophysical Research: Space Physics*, *122*(2), 2398-2423.
775 https://doi.org/10.1002/2016JA023260
776 Durgonics, T., A. Komjathy, O. Verkhoglyadova, E. B. Shume, H.-H. Benzon, A. J. Mannucci,
777 M. D. Butala, P. Høeg, and R. B. Langley (2017), Multiinstrument observations of a
778 geomagnetic storm and its effects on the Arctic ionosphere: A case study of the 19
779 February 2014 storm, *Radio Science*, *52*(1), 146-165.
780 https://doi.org/10.1002/2016RS006106
781 Fuller-Rowell, T., M. Codrescu, R. Moffett, and S. Quegan (1994), Response of the

782 thermosphere and ionosphere to geomagnetic storms, *Journal of Geophysical Research:*
783 *Space Physics*, *99*(A3), 3893-3914. https://doi.org/10.1029/93JA02015
784 Gordon, E. M., A. Seppälä, and J. Tamminen (2020), Evidence for energetic particle
785 precipitation and quasi-biennial oscillation modulations of the Antarctic NO 2 springtime
786 stratospheric column from OMI observations, *Atmos. Chem. Phys.*, *20*(11), 6259-6271.
787 https://doi.org/10.5194/acp-20-6259-2020
788 Karatay, S. (2020), Temporal variations of the ionospheric disturbances due to the seasonal
789 variability over Turkey using IONOLAB-FFT algorithm, *Geodesy and Geodynamics*,
790 *11*(3), 182-191. https://doi.org/10.1016/j.geog.2019.12.002
791 Lei, J., F. Huang, X. Chen, J. Zhong, D. Ren, W. Wang, X. Yue, X. Luan, M. Jia, and X. Dou
792 (2018), Was magnetic storm the only driver of the long-duration enhancements of daytime
793 total electron content in the Asian-Australian sector between 7 and 12 September 2017?,
794 *Journal of Geophysical Research: Space Physics*, *123*(4), 3217-3232.
795 https://doi.org/10.1029/2017JA025166
796 Li, W., J. Yue, Y. Yang, C. He, A. Hu, and K. Zhang (2018a), Ionospheric and thermospheric
797 responses to the recent strong solar flares on 6 september 2017, *Journal of Geophysical*
798 *Research: Space Physics*, *123*(10), 8865-8883. https://doi.org/10.1029/2018JA025700
799 Li, W., D. Zhao, C. He, Y. Shen, A. Hu, and K. Zhang (2021), Application of a Multi-Layer
800 Artificial Neural Network in a 3-D Global Electron Density Model Using the Long-Term
801 Observations of COSMIC, Fengyun-3C, and Digisonde, *SPACE WEATHER*, *19*(3),
802 e2020SW002605. https://doi.org/10.1029/2020SW002605
803 Li, W., D. Zhao, C. He, C. M. Hancock, Y. Shen, and K. Zhang (2022), Spatial-temporal
804 behaviors of large-scale ionospheric perturbations during severe geomagnetic storms on
805 September 7-8 2017 using the GNSS, SWARM and TIE-GCM techniques, *Journal of*
806 *Geophysical Research: Space Physics*, e2021JA029830.
807 https://doi.org/10.1029/2021JA029830
808 Li, W., J. Yue, J. Guo, Y. Yang, B. Zou, Y. Shen, and K. Zhang (2018b), Statistical seismo-
809 ionospheric precursors of M7. 0+ earthquakes in Circum-Pacific seismic belt by GPS TEC
810 measurements, *Advances in Space Research*, *61*(5), 1206-1219.
811 https://doi.org/10.1016/j.asr.2017.12.013

812 Lissa, D., V. K. D. Srinivasu, D. Prasad, and K. Niranjan (2020), Ionospheric response to the
813 26 August 2018 geomagnetic storm using GPS-TEC observations along 80 E and 120 E
814 longitudes in the Asian sector, *Advances in Space Research*, *66*(6), 1427-1440 %@ 0273-
815 1177. https://doi.org/10.1016/j.asr.2020.05.025
816 Mannucci, A., B. Tsurutani, B. Iijima, A. Komjathy, A. Saito, W. Gonzalez, F. Guarnieri, J.
817 Kozyra, and R. Skoug (2005), Dayside global ionospheric response to the major
818 interplanetary events of October 29–30, 2003 "Halloween Storms", *Geophysical Research*
819 *Letters*, *32*(12). https://doi.org/10.1029/2004GL021467
820 Mitchell, C. N., L. Alfonsi, G. De Franceschi, M. Lester, V. Romano, and A. Wernik (2005),
821 GPS TEC and scintillation measurements from the polar ionosphere during the October
822 2003 storm, *Geophysical Research Letters*, *32*(12).
823 https://doi.org/10.1029/2004GL021644
824 Nava, B., J. Rodríguez-Zuluaga, K. Alazo-Cuartas, A. Kashcheyev, Y. Migoya-Orué, S. M.
825 Radicella, C. Amory-Mazaudier, and R. Fleury (2016), Middle-and low-latitude
826 ionosphere response to 2015 St. Patrick's Day geomagnetic storm, *Journal of Geophysical*
827 *Research: Space Physics*, *121*(4), 3421-3438. https://doi.org/10.1002/2015JA022299
828 Ngwira, C. M., J. B. Habarulema, E. Astafyeva, E. Yizengaw, O. F. Jonah, G. Crowley, A.
829 Gisler, and V. Coffey (2019), Dynamic response of ionospheric plasma density to the
830 geomagnetic storm of 22-23 June 2015, *Journal of Geophysical Research: Space Physics*,
831 *124*(8), 7123-7139. https://doi.org/10.1029/2018JA026172
832 Qian, L., W. Wang, A. G. Burns, P. C. Chamberlin, A. Coster, S. R. Zhang, and S. C. Solomon
833 (2019), Solar flare and geomagnetic storm effects on the thermosphere and ionosphere
834 during 6–11 September 2017, *Journal of Geophysical Research: Space Physics*, *124*(3),
835 2298-2311. https://doi.org/10.1029/2018JA026175
836 Ramsingh, S. Sripathi, S. Sreekumar, S. Banola, K. Emperumal, P. Tiwari, and B. S. Kumar
837 (2015), Low-latitude ionosphere response to super geomagnetic storm of 17/18 March
838 2015: Results from a chain of ground-based observations over Indian sector, *Journal of*
839 *Geophysical Research: Space Physics*, *120*(12), 10,864-810,882.
840 https://doi.org/10.1002/2015JA021509
841 Richmond, A., and G. Lu (2000), Upper-atmospheric effects of magnetic storms: a brief tutorial,

Journal of Atmospheric and Solar-Terrestrial Physics, *62*(12), 1115-1127. https://doi.org/10.1016/S1364-6826(00)00094-8

Sheng, C., G. Lu, S. C. Solomon, W. Wang, E. Doornbos, L. A. Hunt, and M. G. Mlynczak (2017), Thermospheric recovery during the 5 April 2010 geomagnetic storm, *Journal of Geophysical Research: Space Physics*, *122*(4), 4588-4599. https://doi.org/10.1002/2016JA023520

Shreedevi, P., R. Choudhary, S. V. Thampi, S. Yadav, T. Pant, Y. Yu, R. McGranaghan, E. G. Thomas, A. Bhardwaj, and A. Sinha (2020), Geomagnetic Storm-Induced Plasma Density Enhancements in the Southern Polar Ionospheric Region: A Comparative Study Using St. Patrick's Day Storms of 2013 and 2015, *Space Weather*, *18*(8), e2019SW002383. https://doi.org/10.1029/2019SW002383

Spogli, L., D. Sabbagh, M. Regi, C. Cesaroni, L. Perrone, L. Alfonsi, D. Di Mauro, S. Lepidi, S. A. Campuzano, and D. Marchetti (2021), Ionospheric response over Brazil to the August 2018 geomagnetic storm as probed by CSES-01 and Swarm satellites and by local ground-based observations, *Journal of Geophysical Research: Space Physics*, *126*(2), e2020JA028368. https://doi.org/10.1029/2020JA028368

Strickland, D. J., R. E. Daniell, and J. D. Craven (2001), Negative ionospheric storm coincident with DE 1-observed thermospheric disturbance on October 14, 1981, *Journal of Geophysical Research: Space Physics*, *106*(A10), 21049-21062. https://doi.org/10.1029/2000JA000209

Walach, M. T., A. Grocott, and S. E. Milan (2021), Average Ionospheric Electric Field Morphologies during Geomagnetic Storm Phases, *Journal of Geophysical Research: Space Physics*, *126*(4), e2020JA028512. https://doi.org/10.1029/2020JA028512

Zhang, R., L. Liu, H. Le, and Y. Chen (2019), Equatorial ionospheric electrodynamics over Jicamarca during the 6–11 September 2017 space weather event, *Journal of Geophysical Research: Space Physics*, *124*(2), 1292-1306. https://doi.org/10.1029/2020JA028512